A Thermoelectrical Approach for the Modelling of Different Ledge Regions in Aluminum Reduction Cells

André Felipe Schneider[1], Daniel Richard[2], Asbjørn Solheim[3] and Marc Dupuis[4]
1. Numerical Analysis Specialist – Center of Excellence for Aluminum, Hatch Ltd., Montréal, Canada
2.Associate – Center of Excellence for Aluminum, Hatch Ltd., Saguenay, Canada
3. Chief Scientist – SINTEF, Trondheim, Norway
4. Consultant, GeniSIM, Inc., Saguenay, Canada
Corresponding author: andre.schneider@hatch.com

Abstract

The energy balance of an aluminum reduction cell largely determines its operational window. A critical design concept is to dissipate enough heat to maintain a frozen layer of electrolyte (the ledge) that will protect the lateral surfaces of the lining from the aggressive bath. Experimental evidence shows that the upper ledge (facing bath) and the lower ledge (facing metal) have different chemical compositions. While the alumina content of the upper ledge is normally lower than in the bulk of the bath, the lower ledge is formed from an Al_2O_3-saturated solution close to the eutectic point. It is rationalized that this is the result of different mechanisms: the top portion is formed by direct freezing of the bulk bath, but the lower ledge originates from an entrained thin film of bath. However, most published energy balance models assume that the heat flux on the entire ledge surface is driven by a single superheat (*i.e.*, the difference between the bulk bath temperature and the liquidus temperature evaluated at the bulk bath composition). This paper proposes a methodology to converge the ledge profile using different melting temperatures for the distinct cavity regions, including a simplified representation of the ledge trench found at the bath-metal interface. This was implemented in the modernized ANSYS-based thermoelectrical model presented earlier [1]. The implications of this paradigm shift in the thermal design of an aluminum reduction cell are discussed by means of the numerical results obtained for a fictitious 300 kA cell technology.

Keywords: Aluminum reduction cells, Heat balance, Ledge trench, Liquidus temperature, Eutectic point.

1. Introduction

The energy balance of an aluminum reduction cell largely determines its operational window. A critical design concept is to dissipate enough heat to maintain a frozen layer of electrolyte (the ledge) that will protect the lateral surfaces of the lining from the aggressive bath. The prediction of the ledge profile can be quite challenging and numerical modeling is broadly employed to study the thermal-electrical behavior of the lining. The authors introduced in 2020 a modernized ANSYS-based thermoelectrical (TE) model [1] that builds upon the foundations first introduced and further developed by Dupuis [2–4] from the mid-1980s up to his most recent publications in the 2020s.

Dupuis' original approach relies on the iterative repositioning of the ledge front in a TE Finite Element (FE) model. The algorithm involves successive repositioning of the solidification front nodes based on the calculated temperature field until the entire ledge-to-liquids interface reaches the bath solidification temperature, T_{liq}. The superheat (*i.e.*, the difference between the bulk bath temperature and the liquidus temperature evaluated at the bulk bath composition, $\Delta T_{upper} = T_{opr} - T_{liq}$), is also adjusted while converging the ledge profile to minimize the difference between the cell internal heat generation and the integrated heat losses over the control volume.

This widely accepted methodology (and variants) assumes that the heat flux on the entire ledge surface is driven by a single superheat.

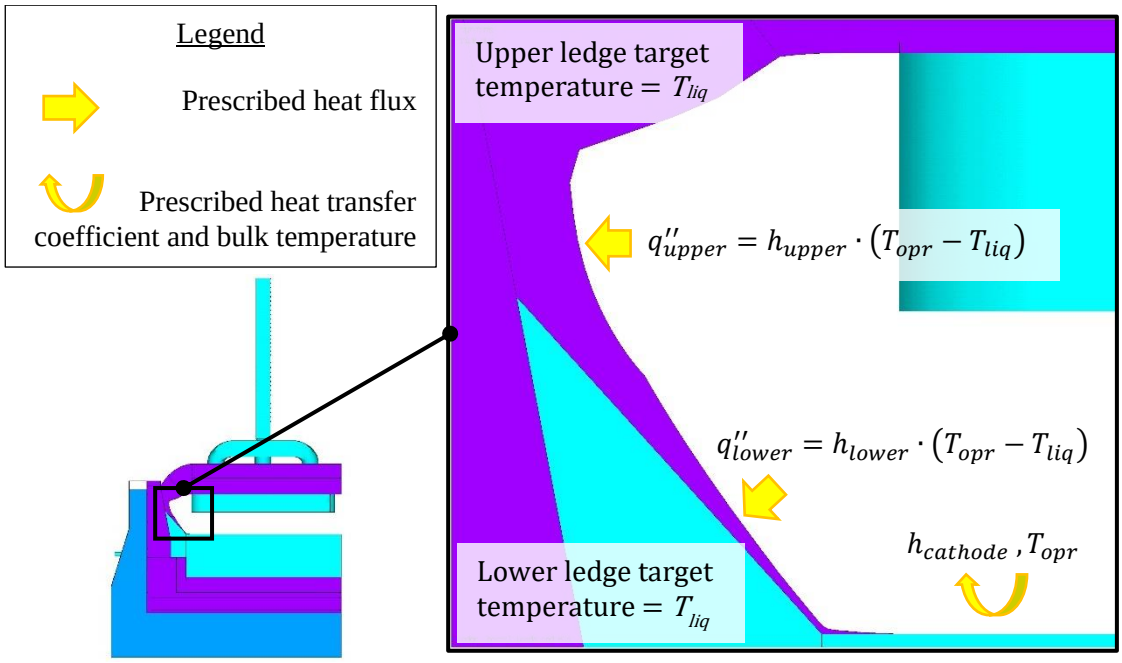

Figure 1. Upper ledge, lower ledge, and cathode panel thermal loads for a traditional FE-based energy balance model.

where:

q''_{upper} Prescribed heat flux at the upper ledge (facing bath), W/m^2

h_{upper} Uniform heat transfer coefficient at the upper ledge (facing bath), W/m^2·°C

T_{opr} Bulk bath temperature, °C

T_{liq} Liquidus temperature evaluated at the bulk bath composition, °C

q''_{lower} Prescribed heat flux at the lower ledge (facing metal), W/m^2

h_{lower} Uniform heat transfer coefficient at the lower ledge (facing metal), W/m^2·°C

$h_{cathode}$ Prescribed uniform heat transfer coefficient at the cathode panel surface, W/m^2·°C.

It is worth noting that this computational strategy is the basis for several successful aluminum reduction technologies designed by different parties, therefore unquestionably valuable from a design standpoint. Nevertheless, experimental evidence suggests that it cannot capture all the features of an industrial cell's ledge profile, as depicted in Figure 2. While models based on this strategy are able to capture the position of the ledge toe fairly well, the lower ledge (facing metal) tends to be either thicker or thinner than the computed profile. Most apparent is a remarkable reduction in the ledge thickness observed at the metal pad-bath interface. Finally, the upper portion (facing bath) of the measured ledge profile tends to be thicker than model predictions.

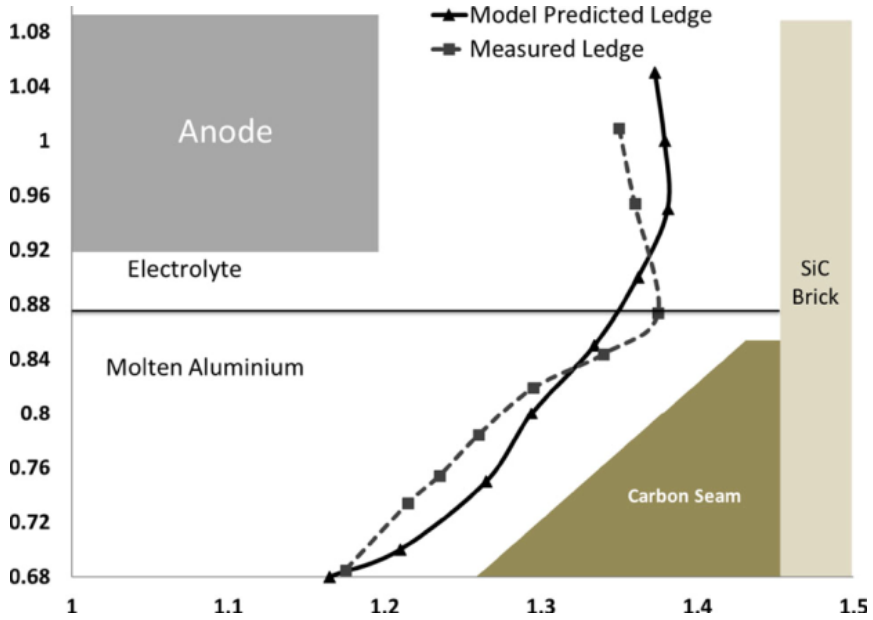

Figure 2. Ledge profile comparison for model prediction vs measurement for an end-to-end aluminum reduction technology (reproduced from [7]).

2. Ledge Formation

The term "ledge" covers different types of frozen material with different chemical compositions formed from the bath (Figure 3). While the alumina content of the upper ledge is normally lower than in the bulk of the bath, the lower ledge is formed from an Al_2O_3-saturated solution close to the eutectic point.

The upper ledge (facing bath) consists of cryolite and small amounts of other bath constituents, and it is formed by near equilibrium freezing of the bath. Freezing and melting is controlled by the product of heat transfer coefficient h_{upper} and the bath superheat, ΔT_{upper} [8]. The heat transfer coefficient h_{upper} can vary spatially with the bath flow profile around the cell. The bath superheat ΔT_{upper} may also vary around the periphery of the cell, mainly due to non-uniform alumina distribution. There is a critical zone around the interface between the bath and the metal pad, known as the "trench", caused by very high local heat transfer coefficient due to interfacial waves (see Figure 3). According to Solheim *et al*. (2019) [9]:

"Fraser et al. […] analysed the shape of the sideledge using a mathematical model, and it was found that the trench ("pinching") could be reproduced by assuming a local heat transfer coefficient of 3000–4000 W/m^{2}K, while the heat transfer coefficient was 800 W/m^{2}K elsewhere."

It is also noteworthy that the ledge trench has a low alumina content, similar to that of the upper ledge (facing bath) and, as a consequence, Solheim *et al*. (2009) [10] proposes that it should be considered as a part of the upper ledge.

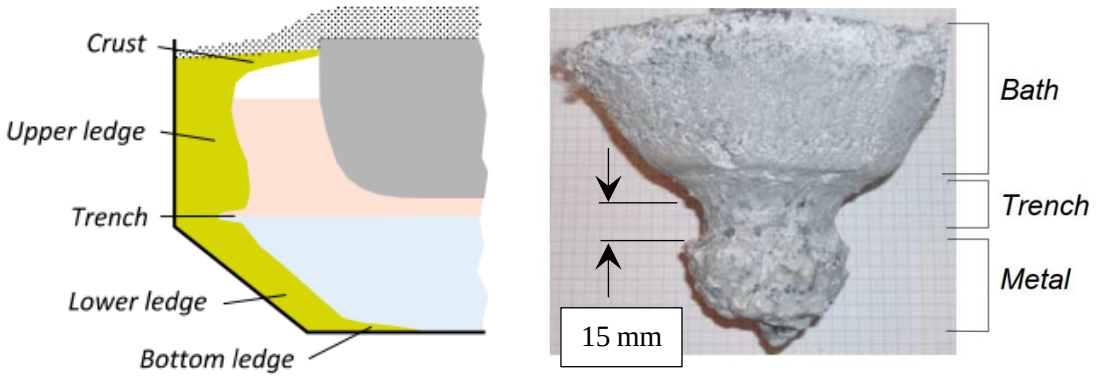

Figure 3. Different types of frozen material that are commonly referred to as "ledge". Left: identification of different ledge regions (reproduced from [9]), Right: 15 mm wide trench obtained with a cold finger device in a lab-scale pot (reproduced from [10]).

The lower ledge (facing metal), on the other hand, contains high concentrations of alumina (27–44 wt% [9]) and appears to be formed by another mechanism. It was suggested that it freezes out from an alumina saturated bath film moving upwards along the ledge, and it is quite possible that solid particles are carried with the film – refer to Solheim *et al.* (2016) [11] for a detailed mathematical description of the phenomenon.

The bath film most likely originates from sludge at the cell bottom and contains less excess AlF_3 than the bulk of the bath. According to Taylor *et al*. [12] and Geay *et al*. [13], this bath film excess AlF_3 concentration is in the range of 0.5 to 5.0 wt% (with 3 wt% on average) and is apparently independent of the bulk bath composition. Since the film is saturated in alumina, it is at its liquidus temperature by definition, and a superheat in the traditional sense cannot be defined. It is proposed that the bath film temperature facing the liquid metal is the eutectic temperature at the film chemistry, such that a lower ledge superheat driving the heat transfer from the metal pad to the ledge at metal level, ΔT_{lower}, is defined according to Equation (1):

$$\Delta T_{lower} = T_{alu} - T_{eut} \qquad (1)$$

where:
ΔT_{lower} Lower ledge superheat, °C
T_{alu} Bulk metal pad temperature, °C
T_{eut} Eutectic point evaluated at the bath film composition, °C.

While the traditional strategy to solve the cell heat balance assumes the metal pad to be at the same temperature than the bulk of the bath, measurements in industrial cells, as shown in Figure 4, reveal that the bulk metal pad temperature T_{alu} is usually 2 °C to 5 °C lower than that of the bulk bath T_{opr}, except at the beginning of the overfeed, when the bulk of the bath becomes colder than the metal pad for a brief period [14]. The measurements also show that T_{alu} not only varies as a function of time, but also spatially within the cavity. These variations are however somewhat dampened compared variation in T_{opr}, most likely since liquid aluminum is a better heat conductor than the bath, and the metal pad does not have intense localized Joule heat generation nor zones of cold material addition.

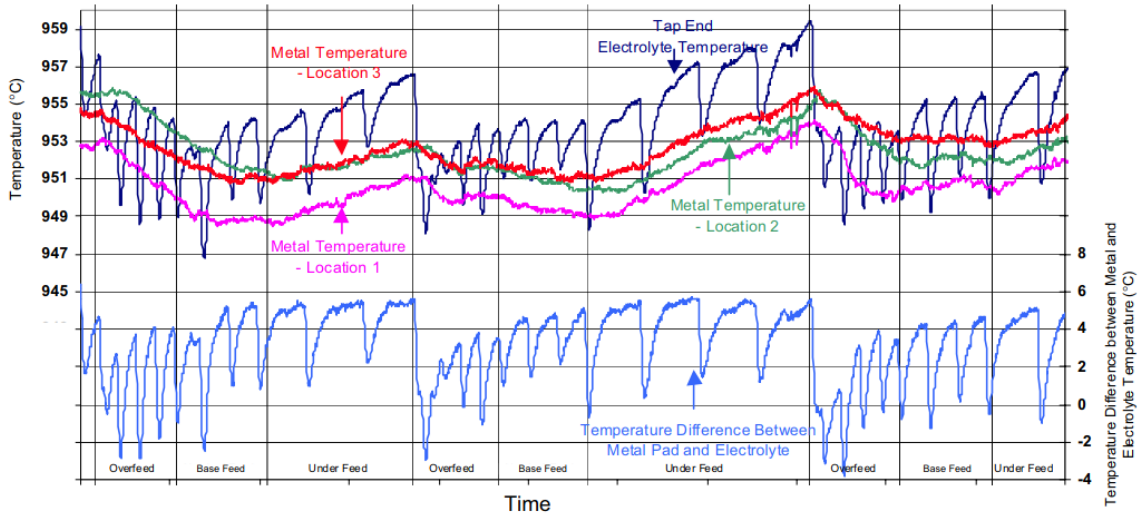

Figure 4. Difference between electrolyte and metal pad temperature over feed cycle (reproduced from [14]).

3. Implementation in the Modernized TE FE Model

A simplified computational approach capable of representing the different ledge regions discussed above was implemented by leveraging the data structure at the core of the modernized TE FE model presented in an earlier publication [1]. The following features were considered during the development:

- The problem is steady state. As a result, the chemical composition of the bulk of the bath and of the bath film do not vary with time, nor do the ledge melting temperatures.
- The time and space-averaged temperature difference between the bulk bath and the bulk metal pad may be computed according to Equation (2):

$$T_{alu} = T_{opr} - \Delta T_{opr-alu} \qquad (2)$$

where:
$\Delta T_{opr-alu}$ is a constant average temperature offset between bulk bath and bulk metal pad temperatures, °C.

- The upper ledge (facing bath) is formed by the direct freezing of the bulk bath and its melting temperature is the liquidus temperature T_{liq} evaluated at bulk bath composition.
- The heat flux between the bulk bath and the upper ledge is a function of the bath superheat ΔT_{upper} and the uniform heat transfer coefficient h_{upper}.
- Given that the ledge trench should be regarded as part of the upper ledge:
  - Its chemical composition is assumed to be the same than the upper ledge;
  - T_{liq} is considered to be the relevant melting temperature for the trench region.
- The heat flux between the liquid phases and the ledge trench is a function of the bath superheat ΔT_{upper} and h_{trench}, [W/m^2·°C], assumed to be a parabolic heat transfer coefficient distribution within the trench region:
  - It varies from h_{lower} at the lower ledge-to-trench interface, reaches its peak value at the trench mid-height and decreases back to h_{upper} at the trench-to-upper ledge interface. This feature was implemented to avoid a large discontinuity in applied heat fluxes on either side of the interfaces.

- The lower ledge (facing metal) is formed from an Al_2O_3-saturated solution originating from the cathode panel and its melting temperature is the eutectic point T_{eut} evaluated at bath film composition.
- The heat flux between the bulk metal pad and the lower ledge is a function of the metal pad superheat ΔT_{lower} and the uniform heat transfer coefficient h_{lower}.
- The heat transfer between the liquid aluminum and the cathode panel is a function of the uniform heat transfer coefficient $h_{cathode}$ and the bulk metal pad temperature T_{alu}.
- Finally, the ledge melting temperatures T_{liq} and T_{eut} are evaluated according to the equations proposed by Solheim *et al*. (1996) [15] and Skybakmoen *et al*. (1997) [16].

Figure 5 depicts the heat transfer loads considered at the cathode panel and at the different ledge regions.

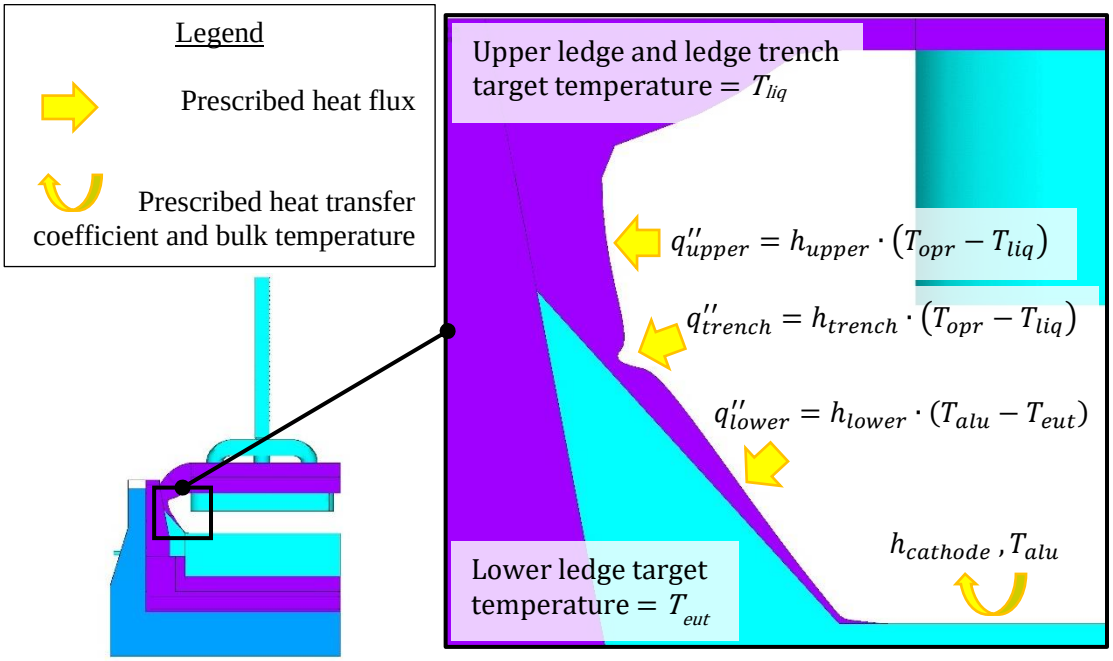

Figure 5. Upper ledge, trench, lower ledge and cathode panel thermal loads for the modernized FE-based energy balance model.

where:

q''_{trench} Prescribed heat flux at the trench region, W/m^2

h_{trench} Parabolic heat transfer coefficient distribution that varies with the trench height, W/m^2·°C.

4. Numerical Experiments

To illustrate the impact of these modifications, four analyses were performed based on a fictitious 300 kA demonstration cell model solved with the modernized TE FE model [1]. Starting with the traditional FE-based energy balance approach, the proposed modifications to the model were introduced one-by-one to assess the impact of each change. Table 1 summarizes the test cases.

Table 1. Test cases description.

Case #	Description	Bath Film	Ledge Trench
1	Traditional FE-based energy balance approach (Figure 1)	Excluded	Excluded
2	Same as Case 1 + inclusion of bath film	$\Delta T_{opr-alu} = 2$ °C	
3	Same as Case 2 + inclusion of ledge trench (Figure 5)		15 mm wide*
4	Same as Case 3 + increment of $\Delta T_{opr-alu}$	$\Delta T_{opr-alu} = 4$ °C	

** The ledge trench is centered around the bath-metal pad interface, according to Figure 3.*

The main process and heat transfer parameters for each analysis are summarized in Table 2. Note that the chemical compositions and the anode-cathode distance (ACD) for Cases 2 through 4 were adjusted to obtain approximately the same internal heat than Case 1. It is also worth mentioning that both h_{upper} and h_{lower} in Case 1 were adjusted to obtain the desired ledge profile.

Table 2. Main process and heat transfer parameters.

		Value			
Parameter	**Unit**	**Case 1**	**Case 2**	**Case 3**	**Case 4**
Cell amperage	kA	300.0			
External voltage	mV	200.0			
ACD	mm	50.2	48.5		
Anode cover thickness		160.0			
Ambient temperature	°C	20			
Bulk bath composition					
Excess (dissolved) [AlF_3]	%	10.825	11.000		
Dissolved [Al_2O_3]		2.500	2.300		
[CaF_2]		3.000*	5.500		
[LiF]		0.00			
[MgF_2]					
Bath film composition					
Excess (dissolved) [AlF_3]	%	-	3.000		
Dissolved [Al_2O_3]			9.100		
[CaF_2]			4.000		
[LiF]			0.000		
[MgF_2]					
Upper ledge (facing bath) heat transfer parameters					
Uniform heat transfer coefficient, h_{upper}	W/m^2·°C	1600	800		
Bulk temperature	°C	T_{opr}			
Solidification front target temperature		T_{liq}			
Ledge trench heat transfer parameters					
Parabolic heat transfer coefficient distribution, h_{trench} (function of trench height)					

		Value			
Parameter	**Unit**	**Case 1**	**Case 2**	**Case 3**	**Case 4**
Lower ledge-to-trench interface	W/m^2·°C	-		h_{lower} = 800	
Ledge trench mid-height				3500	
Trench-to-upper ledge interface				h_{upper} = 800	
Bulk temperature	°C			T_{opr}	
Solidification front target temperature				T_{liq}	

Lower ledge (facing metal) heat transfer parameters			
Uniform heat transfer coefficient, h_{lower}	W/m^2·°C	2100	800
Bulk temperature	°C	T_{opr}	T_{alu}
Solidification front target temperature	°C	T_{liq}	T_{eut}

Cathode panel heat transfer parameters			
Uniform Heat transfer coefficient, $h_{cathode}$	W/m^2·°C	1500	
Bulk temperature	°C	T_{opr}	T_{alu}

** Even though not representative of most aluminum reduction cell technologies, the reported CaF_2 content was kept as indicated to ensure consistency with previously published data.*

Note that all calculations were performed with the same material properties, except for the bulk bath and bath film chemical compositions as per Table 2. Also, the novel ledge topology, first introduced by the authors in [1], was used with 5 rows of 1st order elements across the ledge thickness (Figure 6).

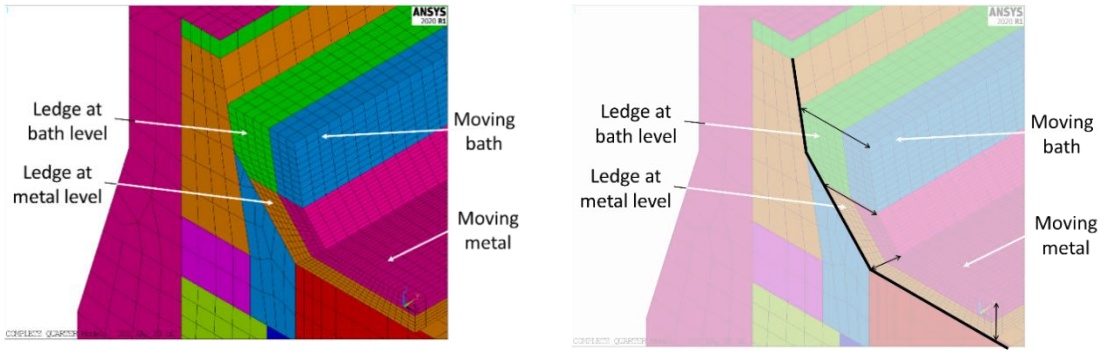

Figure 6. Initial FE mesh and ledge displacement direction for novel ledge topology. Left: initial mesh, Right: ledge displacement direction (reproduced from [1]).

The ledge nodes were iteratively repositioned until the root mean square of the solidification front temperature error was below the RMS convergence norm, *i.e.*, $\varepsilon_{RMS} \leq 0.5$ °C, with a maximum allowable error for any individual node, *i.e.*, an infinite norm $\varepsilon_{INF} \leq 2.0$ °C. Note that only the nodes where the ledge is locally formed were included in the error assessment or, in other words, every node where the ledge is locally melted (*i.e.*, switched to liquid aluminum) was excluded from the error computation.

Figure 7 and Figure 8 show the target temperature and error on solidification front temperature for all eligible nodes for Case 1 and Case 3, respectively.

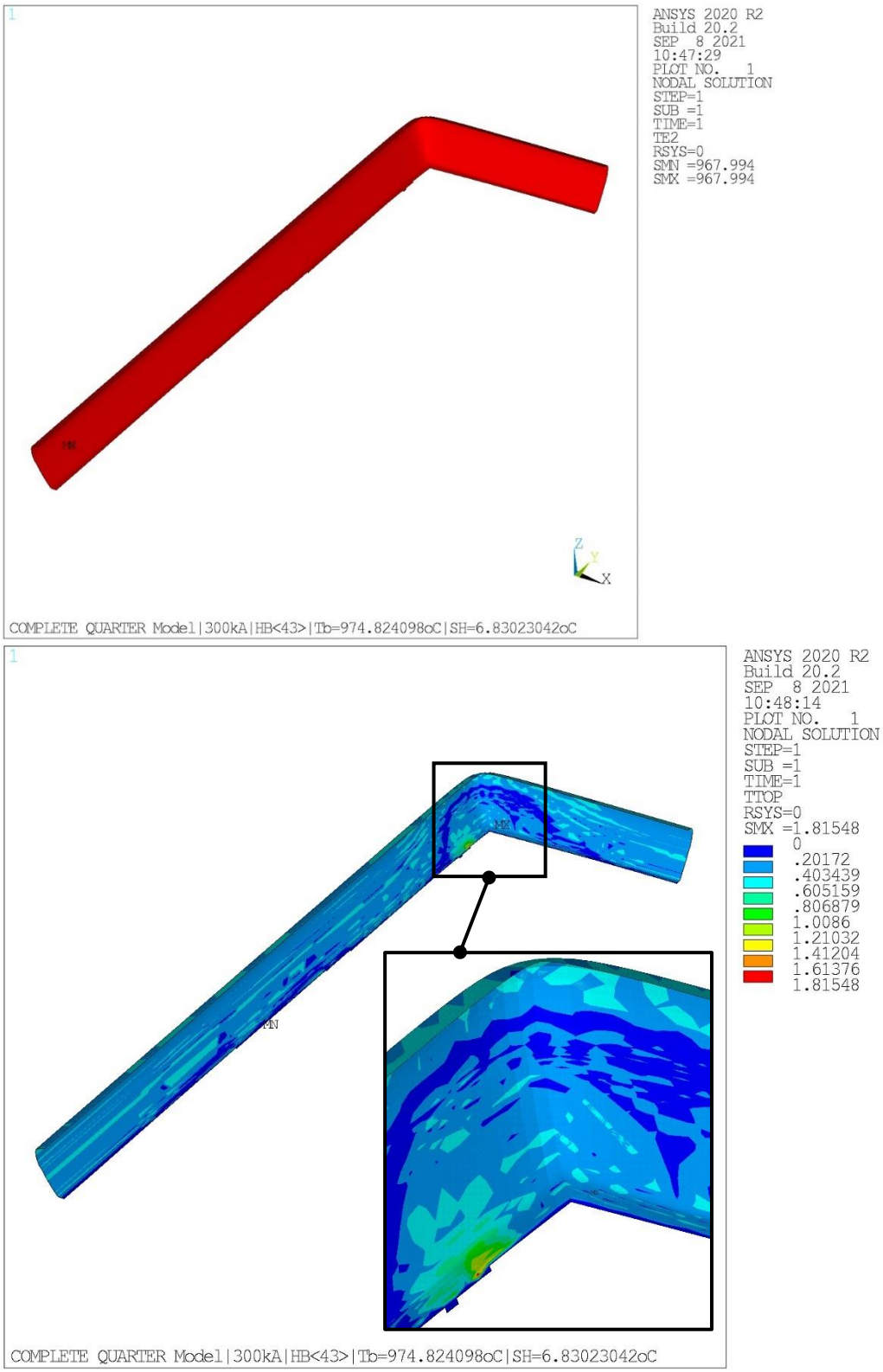

Figure 7. Target temperature and error on solidification front temperature distributions for Case 1, (°C). Top: target temperature, Bottom: error on temperature.

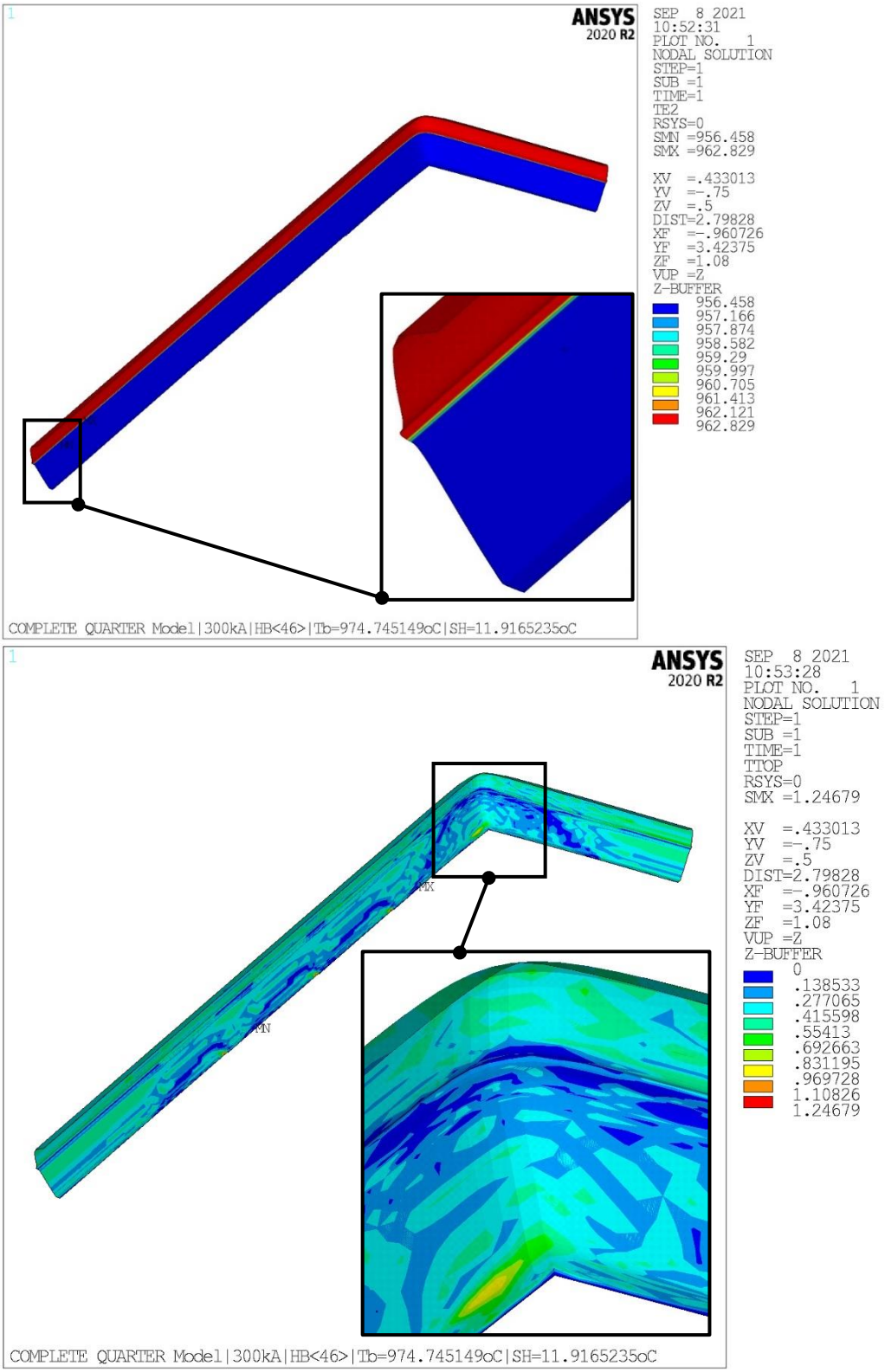

Figure 8. Target temperature and error on solidification front temperature distributions for Case 3, (°C). Top: target temperature, Bottom: error on temperature.

4.1 Main Energy Balance Results

Table 3 summarizes the main energy balance results for all four cases. Comparing the internal heat generation (within ± 0.05 %) and anode-to-cathode heat losses split (within ± 0.45 %), we conclude that these cases are comparable.

Table 3. Main energy balance results.

Result	Unit	Case 1	Case 2	Case 3	Case 4
Bulk bath temperature, T_{opr}	ºC	974.8	976.4	974.7	975.3
Liquidus temperature evaluated at bulk bath composition, T_{liq}	ºC	968.0	962.8	962.8	962.8
Bath superheat, ΔT_{upper}	ºC	6.8	13.6	11.9	12.5
Bulk metal pad temperature, T_{alu}	ºC	-	974.4	972.7	971.3
Eutectic point evaluated at bath film composition, T_{eut}	ºC	-	956.5	956.5	956.5
Metal pad superheat, ΔT_{lower}	ºC	-	17.9	16.2	14.8
Cell internal heat	kW	643.9	644.3	644.5	644.2
Anode heat losses	kW	233.8	233.0	231.7	232.3
Cathode heat losses	kW	410.1	411.3	412.8	412.0
Bath-to-upper ledge heat losses	kW	100.4	99.7	77.1	81.4
Liquids-to-trench heat losses	kW	-		28.8	32.0
Metal pad-to-lower ledge heat losses	kW	141.1	131.7	125.7	115.8
Metal pad-to-cathode panel heat losses	kW	80.1	91.5	90.5	92.7
Total cell heat losses	kW	643.9	644.3	644.5	644.2
Anode voltage drop	mV	339.4	339.4	339.3	339.4
Cathode voltage drop	mV	290.9	291.2	290.9	290.5
Resulting average heat flux					
Upper ledge average heat flux, q''_{upper}	kW/m^2	10.9	10.9	9.5	10.0
Trench average heat flux, q''_{trench}	kW/m^2	-		27.7	28.7
Lower ledge average heat flux, q''_{lower}	kW/m^2	14.3	14.4	13.0	11.9
Cell heat imbalance	kW	0.02	0.04	0.05	0.01
Ledge RMS temperature norm**, ***	ºC	0.33	0.36	0.36	0.37
Ledge INFINITE temperature norm*, ***	ºC	1.82	1.75	1.25	1.46

** Refers to the maximum absolute computed difference with the local ledge melting temperature for an individual eligible node at the ledge-liquids interface.*

*** Refers to the root mean square difference computed with the local ledge melting temperature for all eligible nodes at the ledge-liquids interface.*

**** All those nodes where the ledge is locally melted (*i.e., *switched to liquid aluminum) are excluded.*

4.2 Impact of Bath Film – Comparison Between Cases 1 and 2

Figure 9 shows the comparison between predicted sidewall (SW) ledge profiles for Cases 1 and 2. It can be seen that the inclusion of the bath film slightly reduced the thickness of the lower ledge. This is a direct consequence of the slight increase in the prescribed average heat flux q''_{lower} (refer to Table 3). Furthermore, the ledge toe is shorter for Case 2 given that the lower ledge melting temperature reduced from T_{liq} to T_{eut}, the latter isotherm being located closer to the

potshell while the former, towards the center of the pot. The upper ledge profile remained essentially untouched, given that q''_{upper} is of the same magnitude in both cases. Finally, note that Case 2 was developed to be directly comparable to Case 1.

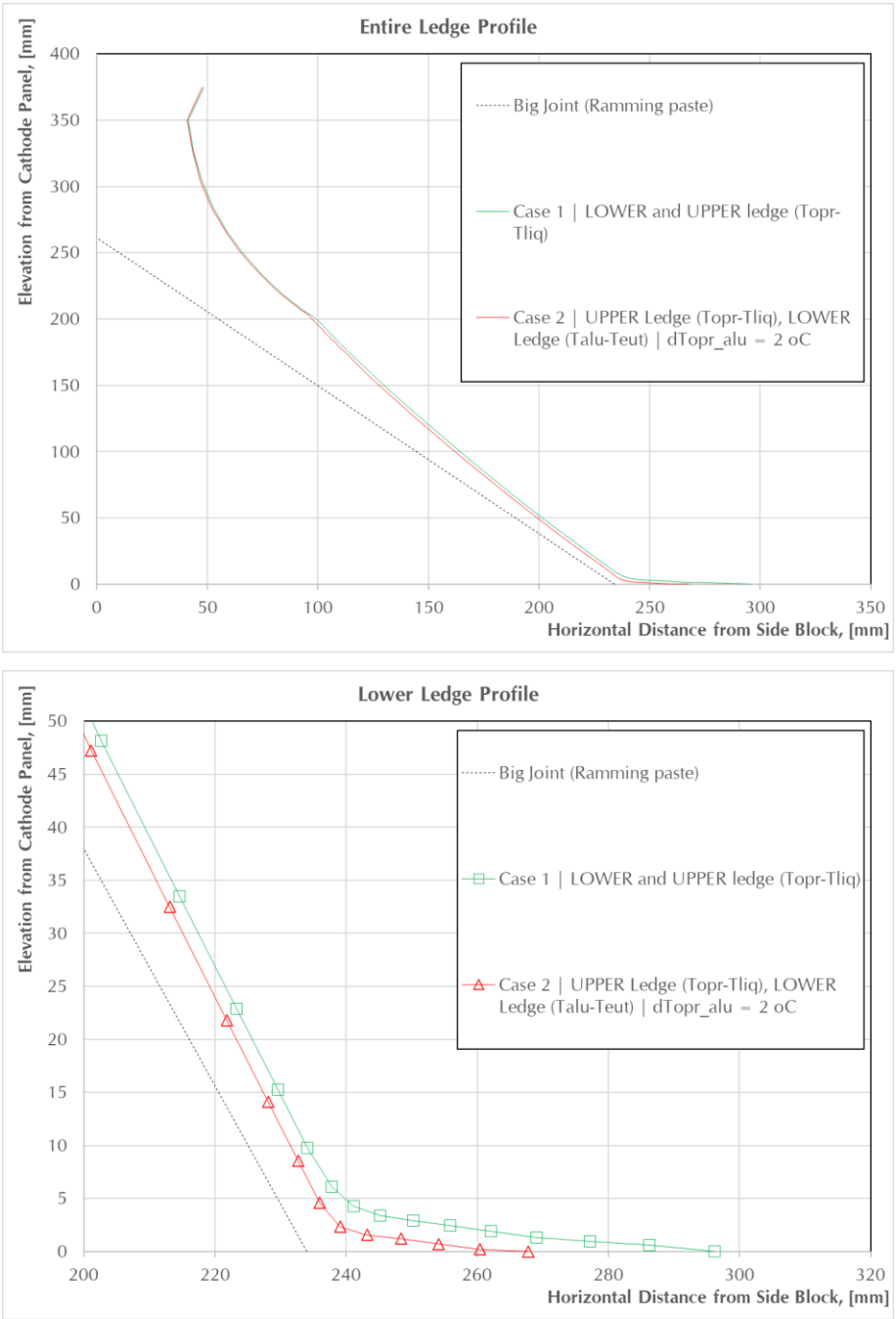

Figure 9. Computed SW ledge profiles for Cases 1 and 2. Top: entire ledge profile, Bottom: lower ledge profile (ledge toe vicinity).

4.3 Impact of Ledge Trench – Comparison Between Cases 2 and 3

Figure 10 illustrates the comparison between predicted sidewall (SW) ledge profiles for Cases 2 and 3. It is shown that the inclusion of the parabolic heat transfer coefficient distribution h_{trench} is indeed capable of creating a remarkable depression on the ledge profile at the bath-metal

interface. The trench is clearly a vulnerable region of the ledge that should not be ignored when assessing a lining design.

One may also observe that both the upper and lower ledge thicknesses increased compared with Case 2. This is a direct consequence of the considerable increase in the heat losses at the bath-metal interface vicinity. Since a larger energy flux is flowing through the trench region (q''_{trench}), lower heat fluxes must exist at the upper (q''_{upper}) and lower (q''_{lower}) ledge regions to maintain the energy balance (refer to Table 3). Consequently, the ledge toe extends further towards the cell center.

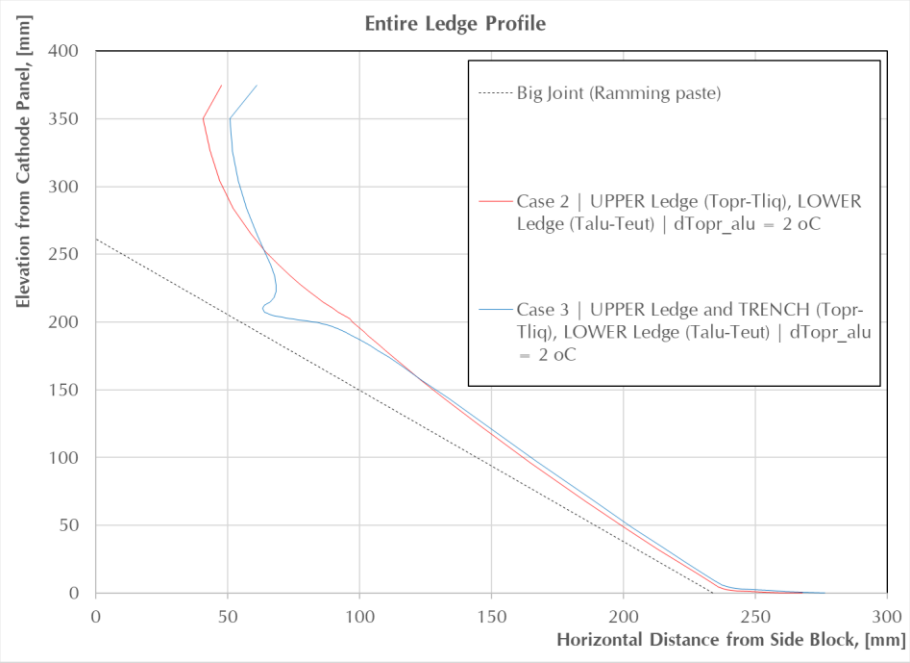

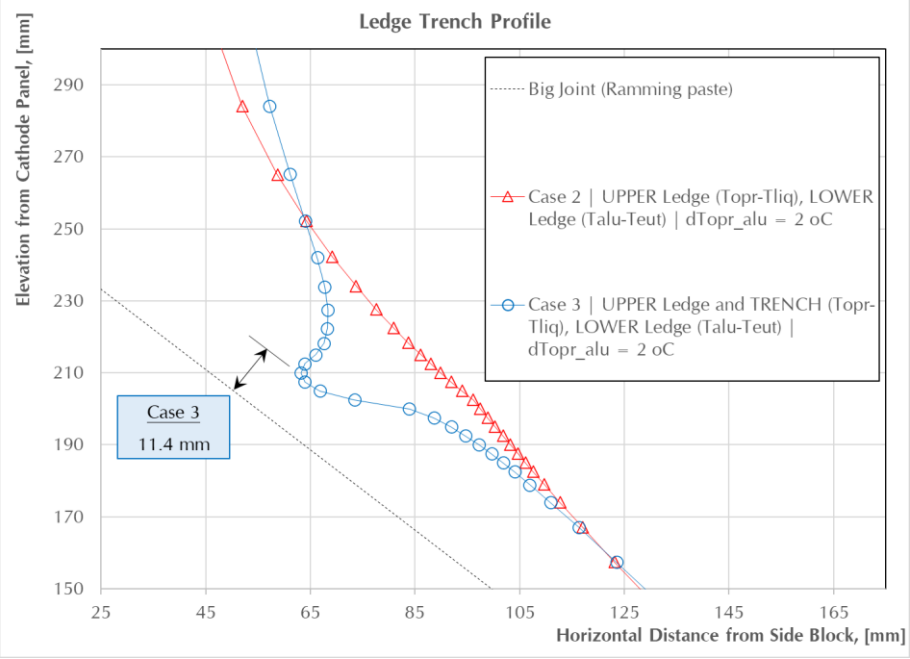

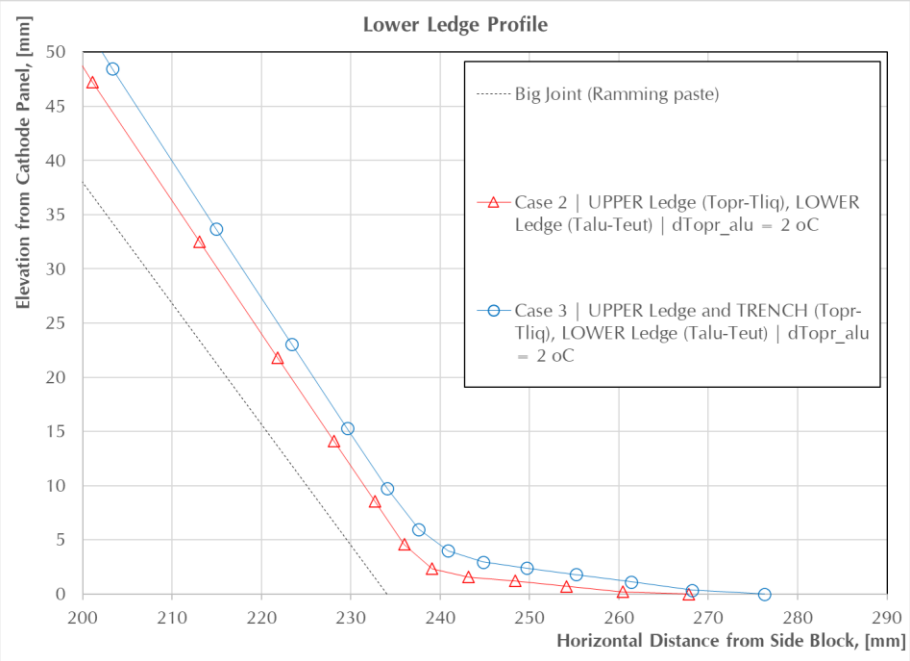

Figure 10. Computed SW ledge profiles for Cases 2 and 3. Top: entire ledge profile, Centre: ledge trench profile, Bottom: lower ledge profile (ledge toe vicinity).

4.4 Impact of Metal Pad Superheat, ΔT_{lower} – Comparison Between Cases 2 and 4

Figure 11 shows the comparison between predicted sidewall (SW) ledge profiles for Cases 2 and 4. The reduction of the metal pad superheat ΔT_{lower} introduced in Case 4 (see Table 3) tends to create a bulge in the lower ledge, extending the ledge toe even further towards to cell center (refer to the results shown in Figure 10).

The change in the ledge profile observed from Case 2 to Case 4 presents a remarkable similarity to the trend shown in the data published by Gupta and Basu (2019) [7], reproduced in Figure 2. This suggests that an adequate description of the overall behavior of the ledge requires both the inclusion of the trench and a reasonable estimation of the metal pad superheat, which is a function of both the bulk metal pad temperature and the bath film chemical composition.

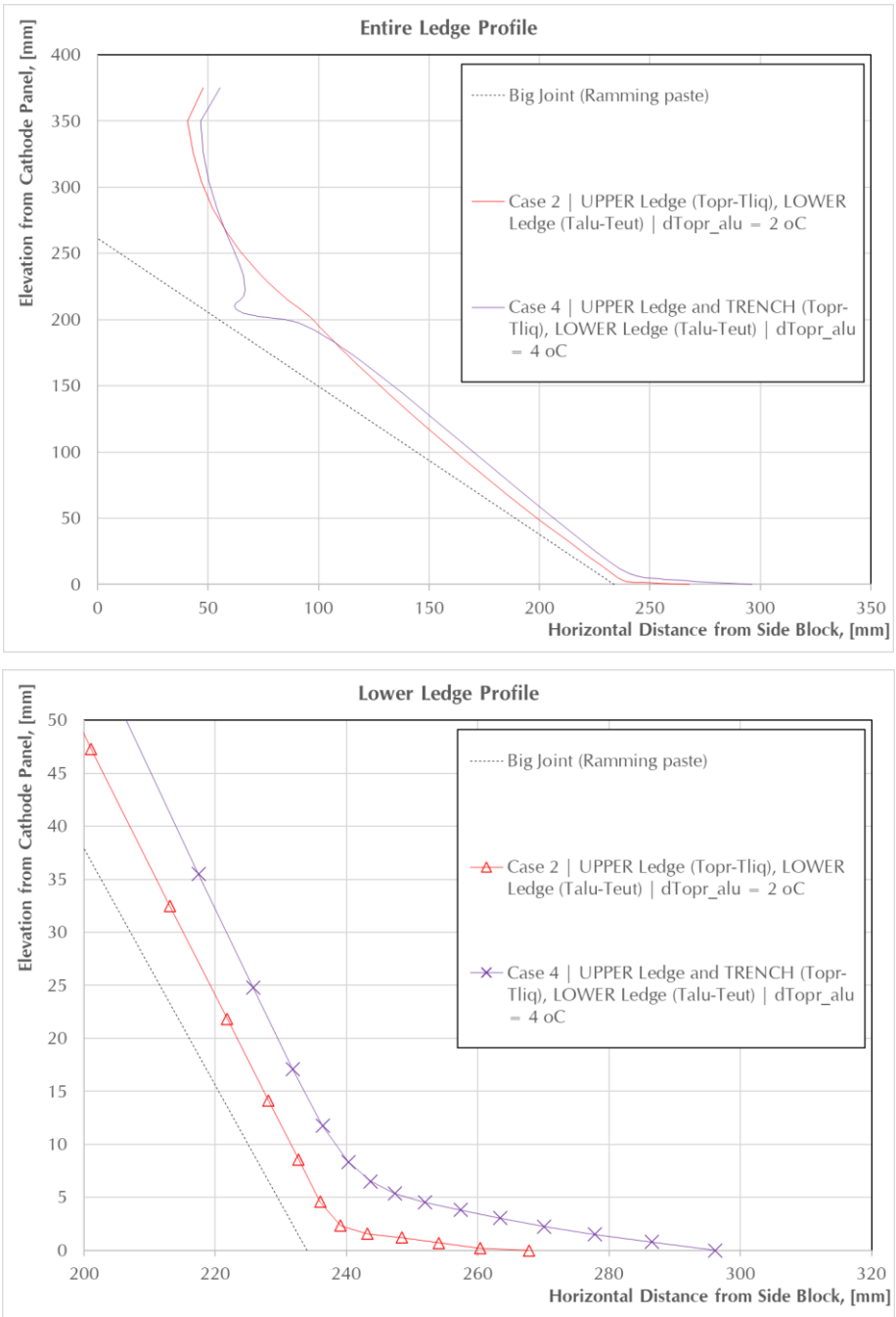

Figure 11. Computed SW ledge profiles for Cases 2 and 4. Top: entire ledge profile, Bottom: lower ledge profile (ledge toe vicinity).

5. Discussion

5.1 On Superheat and Heat Transfer Coefficients

It is well understood that the ledge thickness depends on the heat flux, which depends both on the heat transfer coefficient and on the superheat. It is therefore possible to obtain the right heat flux (hence the right ledge profile) using different combinations of heat transfer coefficients and superheat.

A prebaked cell lining was designed in the past by using the bulk bath eutectic temperature as a basis for the superheat. The heat transfer coefficients h_{upper} and h_{lower} – both calculated by using a measured bulk bath eutectic superheat of about 18 ºC and the measured ledge profile of a prototype cell – were found to be comparable to the published experimental values at the time (*i.e.*, between 530 and 800 W/m^2·K at the bath and metal pad level, respectively).

Note that the bulk bath liquidus superheat at the same bath chemistry corresponded to roughly 6 ºC, or 3 times lower than the eutectic one. This means that, if said prebaked cell lining were to be designed based on the bulk bath liquidus temperature T_{liq}, heat transfer coefficients of h_{upper} = 1600 W/m^2·K and h_{lower} = 2400 W/m^{2}K would be required to obtain identical computed ledge profiles. These coefficients are rather high compared to experimental values, and the large difference between them (*i.e.*, 50 % larger at the metal pad level) is difficult to justify.

It is quite interesting to note that it was deemed more convenient at the time to use the bulk bath eutectic superheat for both upper and lower ledge regions, given that it eliminated the negative liquidus superheat estimations reported in the 1980's while also leading to calibrated heat transfer coefficients that seemed more reasonable than those obtained with the one based on the bulk bath liquidus temperature. However, it was shown that only the bulk bath liquidus superheat could successfully represent the dynamic behaviour of the measured bulk bath temperature evolution in a side broken Söderberg cell [17], Figure 12.

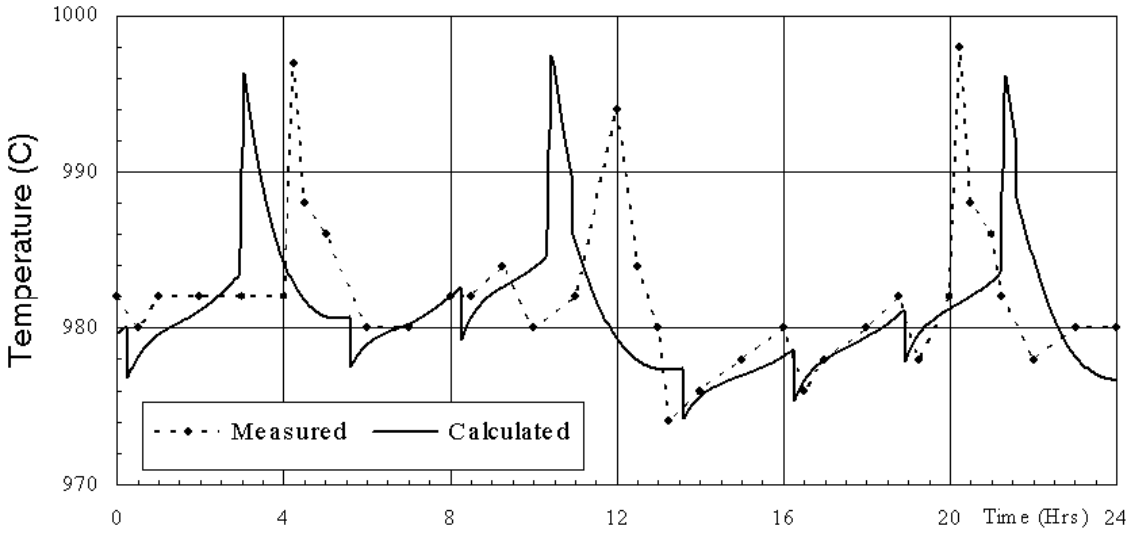

Figure 12. Comparison of measured and calculated bulk bath temperature evolution using bulk bath liquidus superheat, (reproduced from [17]).

This conundrum between liquidus and eutectic superheat seems to be addressed satisfactorily with the new physics implemented in this version of the TE model, *i.e*, using different superheats at the bath and metal level, which results in required heat transfer coefficients at bath and metal level that are reasonable and in line with published experimental data.

5.2 On Bath Film

Regarding the ledge at the metal level, the bath film is probably the main mechanism for removal of sludge, and therefore it is expected that their composition would be similar. As shown in Figure 13, the sludge composition does show some variation [12, 13], but is apparently independent of the bulk bath excess AlF_3 concentration. It is possible that the sludge age is important. It is expected that freshly formed sludge composition will be closer to the bulk bath composition,

while the sodium activity in the metal pad will result in sodium fluoride formation at the bath film at metal level.

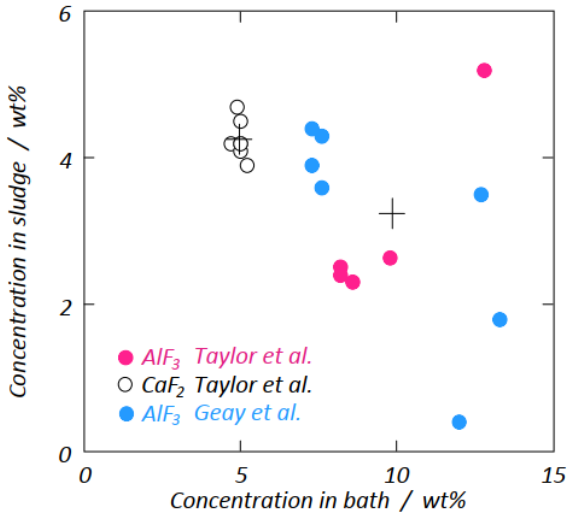

Figure 13. AlF_3 and CaF_2 content in both bulk bath and sludge (reproduced from [11]).

Experimental characterization of the bath film chemistry may possibly be done using a conveniently run-out cell with an "intact" ledge, similarly to the work done in [10].

5.3 On Ledge Trench

Given that normally the thinnest ledge is at the trench, it seems reasonable that it should be considered in lining design work. To the authors' knowledge, there is no experimental evidence suggesting that the trench behaviour would vary significantly with different cell technologies.

One potential avenue towards the experimental verification of the trench would be to study the same conveniently run-out cell with an "intact" ledge.

5.4 Impact on Model Validation and on its Industrial Application

While the proposed modelling strategy is able to reproduce ledge features measured in industrial cells, it does require more input parameters that need to be measured, calibrated and validated before it can be used as a design tool.

The new physics implemented in the modernized ANSYS-based TE model relies on operational parameters that are not easy to measure, *e.g.*, the metal level liquid bath film chemistry, the temperature difference between the bath and the metal pad and the ledge trench profile. During the development of our test cases, it was observed that the model behaviour was very sensitive to the selection of the dissolved alumina concentration in the bulk bath.

Given all these additional difficulties, inherent to the newly implemented physics, it is quite likely that h_{upper}, h_{lower} and h_{trench} will have be calibrated on a case-by-case basis, analogously to the current practice when employing the traditional FE energy balance approach. However, once properly validated, it is the authors' opinion that the model should be a useful cell lining design tool, providing a better assessment of the critical ledge thickness at the bath-metal interface trench.

6. Conclusions

A methodology to converge the ledge profile using different melting temperatures for the distinct cavity regions, including a simplified representation of the ledge trench found at the bath-metal interface was implemented by leveraging the data structure of the modernized ANSYS-based TE FE model previously introduced by the authors. This methodology uses two distinct superheat definitions, namely, the traditional $\Delta T_{upper} = T_{opr} - T_{liq}$ at the bath level, and $\Delta T_{lower} = T_{alu} - T_{eut}$ at the metal pad level. The lower ledge superheat requires a reasonable estimation of both the bulk metal pad temperature and the bath film chemical composition. Finally, the simplified representation of the ledge trench is based on a parabolic heat transfer coefficient distribution that varies with the trench height.

Based on the obtained numerical results, it is the opinion of the authors that computation of a more realistic ledge profile requires considering both the unavoidable trench at the bath-metal interface and the different ledge formation mechanisms at metal pad and bath level. While the preliminary results are encouraging, validation against actual pots is required to determine both its reliability and usefulness as a design tool.

7. References

1. Daniel Richard et al., A modernized ANSYS-based finite element model for the thermal-electrical design of aluminum reduction cells, *Proceedings of the 38th International ICSOBA Conference*, Virtual Event, 16 to 18 November, 2020, Paper AL03, *Travaux* 49, 563-580.
2. Marc Dupuis & Imad Tabsh, Thermo-electric coupled field analysis of aluminium reduction cells using the ANSYS parametric design language, *Proceedings of the ANSYS Fifth International Conference*, Vol 3, 1991, 1780-1792.
3. Marc Dupuis, Thermo-electric design of a 400 kA cell using mathematical models: a tutorial, *Light Metals* 2000, 297-302.
4. Marc Dupuis, Computation of aluminium reduction cell energy balance using ANSYS® finite element models, *Light Metals* 1998, 409-417.
5. Marc Dupuis, Computation of accurate horizontal current density in metal pad using a full quarter cell thermo-electric model, *Proceedings of CIM* 2001, 3-11.
6. Marc Dupuis, How to limit the heat loss of anode stubs and cathode collector bars in order to reduce cell energy consumption, *Light Metals* 2019, 521-531.
7. Amit Gupta and Biswajit Basu, Sustainable primary aluminium production – technology status and future opportunities, *Transactions of the Indian Institute of Metals*, Volume 72, Issue 8, 2019, 2135–2150.
8. Asbjørn Solheim, Some aspects of heat transfer between bath and sideledge in aluminium reduction cells, *Light Metals* 2011, 381-386.
9. Asbjørn Solheim et al., Sideledge in Aluminium Cells: Further Considerations Concerning the Trench at the Metal-Bath Boundary, *Light Metals* 2019, 787-793.
10. Asbjørn Solheim, Henrik Gudbrandsen and Sverre Rolseth, Sideledge in aluminium cells: the trench at the metal-bath boundary, *Light Metals* 2009, 411-416.
11. Asbjørn Solheim, Nils-Håvard Giskeødegård, and Nancy J. Holt, Sideledge facing metal in aluminium electrolysis cells: freezing and melting in the presence of a bath film, *Light Metals* 2016, 333-338.
12. Mark P. Taylor et al., The dynamics and performance of reduction cell electrolytes, *Light Metals* 1990, 259-266.
13. P-Y. Geay, Barry J. Welch, and Pierre Homsi, Sludge in operating aluminium smelting cells, *Light Metals* 2001, 541-547.
14. Daniel Whitfield et al., Metal pad temperatures in aluminium reduction cells, *Light Metals* 2004, 239-244.

15. Asbjørn Solheim et al., Liquidus Temperatures for Primary Crystallization of Cryolite in Molten Salt Systems of Interest for the Aluminium Electrolysis, *Metallurgical and Materials Transactions B*, 27, 1996, 739-744.
16. Egil Skybakmoen, Asbjørn Solheim, and Åsmund Sterten, Alumina Solubility in Molten Salt Systems of Interest for Aluminium Electrolysis and Related Phase Diagram Data, *Metallurgical and Materials Transactions B*, 28, 1997, 81-86.
17. Tabsh, M. Dupuis and A. Gomes, Process Simulation of Aluminum Reduction Cells, *Light Metals* 1996, 451-457.